Frictional strength and strain weakening in simulated fault gouge: Competition between geometrical weakening and chemical strengthening

André Niemeijer,[1,2,3,4] Chris Marone,[2,3] and Derek Elsworth[1,3]

Received 30 December 2009; revised 18 May 2010; accepted 9 June 2010; published 20 October 2010.

[1] Despite the importance of hydromechanical effects in fault processes, not much is known about the interplay of chemical and mechanical processes, in part because the conditions are difficult to simulate in the laboratory. We report results from an experimental study of simulated fault gouge composed of rock salt sheared under conditions where pressure solution is known to operate. At sliding velocities above 10 μm/s and high shear strains (>5), friction measurements show that layers of rock salt weaken significantly and ultimately slide unstably (i.e., stick-slip). Microstructural observations show the presence of a zone of comminuted grains along shear zone boundaries, forming boundary-parallel Y shears at high sliding velocities. Samples deformed at low sliding velocities do not show boundary-parallel shear but rather exhibit low porosity passive regions isolated by dilational zones in the Riedel shear orientation. We posit that the significant strain weakening observed at high sliding velocities is caused by severe grain size reduction as shear localization develops, i.e., by frictional wear, ultimately leading to the development of a throughgoing boundary parallel Y shear. Unstable slip is probably related to rupture on this Y shear surface with intermittent healing of the asperities by pressure solution. Furthermore, the data show that the weakening and subsequent unstable slip can be delayed (i.e., occur at higher strains) by lower sliding velocities, larger initial grain sizes, lower normal stresses, and the presence of fluids. This suggests a competition between mechanical wear and chemical processes. Our data highlight the importance of hydrothermal processes in tectonic faulting.

Citation: Niemeijer, A., C. Marone, and D. Elsworth (2010), Frictional strength and strain weakening in simulated fault gouge: Competition between geometrical weakening and chemical strengthening, *J. Geophys. Res.*, *115*, B10207, doi:10.1029/2009JB000838.

1. Introduction

[2] Fluids play a crucial role in many processes within Earth's crust [e.g., *Byerlee*, 1994; *Hickman and Evans*, 1995] including faulting and emplacement of hydrocarbons and ore deposits [e.g., *Sibson*, 2001]. Fluids are also important in affecting the seismic cycle, either through physical changes in effective stress [*Sibson*, 1973; *Rice*, 1992; *Faulkner and Rutter*, 2001] or via the chemical effects of pressure solution on deformation, fault healing, and sealing of fault gouges [*Rutter and Mainprice*, 1979; *Cox*, 1994; *Bos et al.*, 2000; *Bos and Spiers*, 2002a, 2002b; *Tenthorey et al.*, 2003; *Yasuhara et al.*, 2005; *Niemeijer and Spiers*, 2005, 2006, 2007; *Tenthorey and Cox*, 2006; *Giger et al.*, 2007; *Niemeijer et al.*, 2008a, 2008b]. Despite the known importance of fluids, the complex interplay of mechanical and chemical processes in the crust is poorly understood. Part of this lack of knowledge is due to the technical challenge of recreating the conditions where these processes operate; the processes are too slow to observe over typical laboratory time scales and/or it is difficult to isolate individual processes. However, several experimental studies on simulated fault gouges have been performed under conditions where pressure solution processes may be operating [e.g., *Chester and Higgs*, 1992; *Karner et al.*, 1997; *Bos et al.*, 2000; *Kanagawa et al.*, 2000; *Bos and Spiers*, 2002b; *Tenthorey and Cox*, 2006; *Giger et al.*, 2008; *Niemeijer et al.*, 2008b]. These studies have shown that substantial gouge compaction, via pressure solution processes occurs under hydrothermal conditions and over laboratory time scales. Gouge compaction in the presence of a chemically active pore fluid is associated with lithification and healing, which lead to increased strength and changes in elastic properties. Furthermore, the frictional strength of pure gouges increases with increased activity of pressure

[1]Department of Energy and Mineral Engineering, Pennsylvania State University, University Park, Pennsylvania, USA.
[2]Department of Geosciences, Pennsylvania State University, University Park, Pennsylvania, USA.
[3]G3 Center and Energy Institute, Pennsylvania State University, University Park, Pennsylvania, USA.
[4]Now at Istituto Nazionale di Geofisica e Vulcanologia, Rome, Italy.

0148-0227/10/2009JB000838

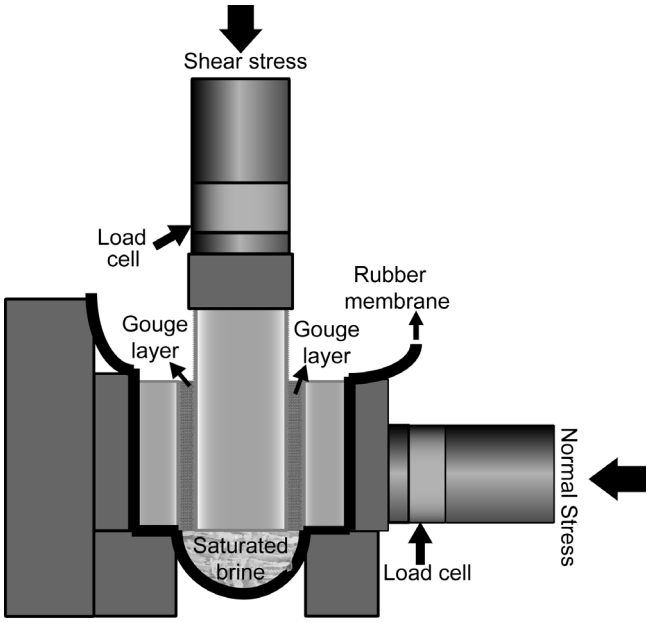

Figure 1. Schematic diagram of the double-direct shear configuration.

solution, presumably due to enhanced densification [*Bos et al.*, 2000; *Kanagawa et al.*, 2000; *Tenthorey and Cox*, 2006]. Conversely, other studies [*Chester and Higgs*, 1992; *Chester*, 1994; *Blanpied et al.*, 1995; *Chester*, 1995] have suggested that pressure solution processes should lead to weakening and a transition from localized to distributed deformation. A recent study by *Giger et al.* [2008] on simulated quartz gouges under hydrothermal conditions demonstrated moderate mechanical weakening under moderately reactive, hydrothermal conditions and significant strain weakening under highly reactive conditions, associated with localization of slip along the rock-gouge interface. They interpreted this to be the result of inhibition of cataclastic granular flow by solution-transfer processes such as dissolution of fine wear material and pressure solution. Their work highlights the complex effects of pressure solution processes on the frictional behavior of fault gouges, especially regarding the velocity and strain dependence of friction.

[3] The purpose of this study is to report on experiments designed to investigate the role of pressure solution and fluid-rock interactions on friction constitutive behavior over a wide range of sliding velocities (0.3–500 μm/s). We study simulated fault gouges with rock salt to promote pressure solution processes. Rock salt is used as a room temperature analogue of chemically activated natural fault rock materials under hydrothermal conditions [*Spiers et al.*, 1990, 2004; *Schutjens and Spiers*, 1999; *Niemeijer et al.*, 2009]. We report on the effects of shear strain, pore fluid chemistry, initial grain size, fault roughness, sliding velocity, and normal stress on the frictional strength of fault gouges.

2. Experimental Approach

[4] In this study we present results from double-direct shear experiments in a biaxial loading configuration (see Figure 1). The samples consist of ground natural rock salt, sieved in three grain size fractions: 38–53, 38–106, and 106–212 μm. Layers of fault gouge were constructed using ~12 grams of material in each of the two layers (nominal frictional contact dimension is 5 × 5 cm), which are placed within a three-block configuration (Figure 1). The layers are sheared by driving the central block down between the two stationary side blocks. Surfaces of the titanium or steel forcing blocks have regularly spaced teeth (average height ~0.8 mm, spacing 1 mm), which provide coupling to the layer and promotion of shear within the layer. The horizontal and vertical loads of the biaxial testing machine produce normal and shear stress, respectively, on the layers (Figure 1). Stresses are measured by load cells with a resolution of 0.1 kN, which translates to ~0.04 MPa for the 5 × 5 cm block faces. Shear and normal displacements of the gouge layer boundaries are measured with Direct Current linear variable Differential Transformers (DCDTs) to a resolution of ±0.1 μm. Our experiments were conducted at layer normal stresses of 2.5–7.5 MPa, sliding velocities measured at the layer boundaries of 0.3–500 μm/s, and fluid conditions from wet to nominally dry (Table 1). Previous work has shown that pressure solution is the dominant deformation mechanism under these stress conditions [*Spiers and Schutjens*, 1990; *Niemeijer et al.*, 2008a, 2009].

[5] Brine-saturated experiments were performed by placing the sample assembly inside a rubber membrane (Figure 1). The sample was left to saturate under load for ~10–120 min. After this initial saturation (absent in the dry experiments), the vertical ram was brought into contact with the center block ("bumped") after which shear displacement was computer-controlled at predescribed velocities. Initial porosity was determined by weighing the amount of material and measuring the thickness of the sample assembly to ±50 μm. Changes in porosity were monitored continuously during shear via measurement of the change in layer thickness (to ±0.1 μm). At the end of the experiments, some samples were removed from the forcing blocks using a razor blade, flushed with iso-butanol and dried for 24 h at 60°C. These samples were impregnated with blue-stained, thin epoxy resin (Buehler Company), and standard thin sections were cut for image analysis and microstructural study using a light microscope and scanning electron microscope.

3. Results

[6] Table 1 summarizes the experiments and their corresponding conditions reported in this paper. We focused primarily on halite particles in the range 38–106 μm (Table 1). We begin by presenting results from experiments performed at constant sliding velocities and then discuss the velocity dependence of strength and links with microstructural observations. Together, these data lead to a conceptual model for deformation mechanisms and the key processes responsible for the observed range of behaviors. We augment the main set of experiments with tests designed to address specific questions, hypotheses, and process-based models.

3.1. Constant Sliding Velocity

[7] For all experiments performed at constant sliding velocity in the presence of saturated brine, the evolution of shear stress and porosity with shear strain is shown in Figures 2 and 3. Each of these tests used particles in the

Table 1. List of Experiments and Corresponding Conditions[a]

Experiment	Grain size (μm)	σ_n (MPa)	v (μm/s)	h_0 (μm)	Displacement (mm)	Shear Strain	Pore Fluid
p1559	38-106	5	10-1-10-3-30-10-100-10	3240	25.90	9.87	brine
p1560	38-106	5	10-100-10-30-3-10-1-10	3198	21.02	7.69	brine
p1573	38-106	5	100	2594	29.93	16.13	brine
p1574	38-106	5	30	2550	29.93	17.11	brine
p1575	38-106	5	0.3	2563	17.94	9.54	brine
p1576	38-106	5	10	2795	29.93	15.73	brine
p1577	38-106	5	30	2734	29.93	15.96	brine
p1578	38-106	5	100	3007	29.93	13.41	brine
p1579	38-106	5	3	2322	29.93	20.50	brine
p1587	38-106	5	1	2927	29.93	17.24	brine
p1593	38-106	5	1	3042	29.93	14.32	brine
p1594	38-106	5	25	3212	29.93	11.51	brine
p1595	38-106	5	20	2999	29.93	12.53	brine
p1596	38-106	5	15	2860	29.93	13.35	brine
p1761	38-106	5	10-100-10-100-10-100	3803	25.24	7.93	brine
p1899	38-106	5	10-100-10-100-10-100	3725	34.91	13.34	brine
p1900	38-106	5	100	3556	29.93	10.42	brine
p1901	38-106	5	100-10-100-10-100-10	3638	29.93	10.35	brine
p1902	38-106	5	100	3782	29.83	11.10	brine
p1922	38-106	5	100	3898	9.98	2.70	brine
p1924	38-106	5	300	3469	29.93	10.51	brine
p1933	38-106	5	500	3302	29.68	11.15	brine
p1934	38-106	5	100	3444	17.33	5.74	brine
p1959	106-212	5	100	3584	29.93	11.22	brine
p1960	38-53	5	100	3533	29.93	10.64	brine
p1961	38-106	5	100	3992	29.93	10.47	humidity
p1962	38-106	5	60	3473	29.93	10.85	brine
p1964	38-106	2.5	100	3127	29.93	12.23	brine
p1965	38-106	7.5	100	3558	29.93	10.56	brine
p1967	38-106	5	100	3974	29.93	10.22	oil
p1993	38-106	5	100	3975	12.20	3.24	brine
p1994	38-106	5	100	3620	13.05	3.80	brine
p1995	38-106	5	100	3301	9.71	3.02	brine
P2011	38-106	5	100	4265	29.93	9.81	room-dry
p2235	38-106—glass beads	5	100	3103	29.93	12.35	brine
p2268	38-106—sand	5	100	3124	29.93	13.19	brine

[a] h_0 refers to the layer thickness at the start of shearing. Experiments p2235 and p2268 were performed with granite blocks roughened by sandblasting with the listed medium.

range 38–106 μm (Table 1). For low sliding velocities (<20 μm/s), we observed an initial peak stress (Figure 2a), accompanied by dilation (Figure 3a), after which samples weaken and finally strengthen again at shear strains above ~3. Quasi steady state strength is usually reached by a shear strain of 5, and frictional strength decreases as sliding velocity increases (Figure 2b). In contrast, at high sliding velocity (>20 μm/s), we observe quite different behavior. After an initial peak in shear stress, a similar weakening and strengthening is observed (Figure 2a), but this is followed by a strong strain weakening and ultimately unstable stick-slip behavior (shown by what looks like noise/spikes in the data, for example, starting at a shear strain of 5 in p1573). Figure 3a shows the evolution of apparent porosity with shear strain for the same set of experiments. Because of the direct shear geometry, layers thin during shear deformation, but we correct for this effect by adding the amount due to thinning to the measured horizontal displacement (for details see *Scott et al.* [1994]).

[8] From Figure 3a, it is apparent that all samples dilate during initial shearing. The amount of dilation depends on the initial porosity at the start of shearing, which in turn depends on the time of saturation under load. In experiments p1573–p1579, the time of saturation under load was 40–50 min, resulting in starting porosities of 16%–21%. Variations in the porosity are presumably due to slight extrusion of material from between the blocks (top and bottom) and shear localization that leads to complexity in shear-induced layer thinning. For later experiments, the saturation time was more variable (between 20 and 40 min), which results in a larger variation of the starting porosity. Despite this variation in initial porosity, it is clear that dilation is promoted by higher sliding velocity. Gouges deformed at low sliding velocity (experiments p1576 and p1579) show a transition from initial dilation to ongoing compaction during shear (Figure 3a).

[9] In Figure 3b we show the porosity at a shear strain of 10, which represents quasi steady state conditions (Figure 3a). Steady state porosity increases with increasing sliding velocity (Figure 3b). This behavior and the corresponding shear-strain dependence (Figure 3a) are analogous to an overcompacted soil that dilates during initial shear. With increasing sliding velocity, dilation increases relative to time-dependent pressure solution compaction, which results in a higher overall porosity. For shearing velocities above ~20 μm/s, porosity remains constant during the periods of unstable stick slip, whereas porosity increases during the strong strain weakening (compare Figures 2a and 3a).

3.2. Velocity Dependence of Strength

[10] We conducted velocity step tests to measure friction rate/state behavior [e.g., *Marone*, 1998]. Typical velocity-

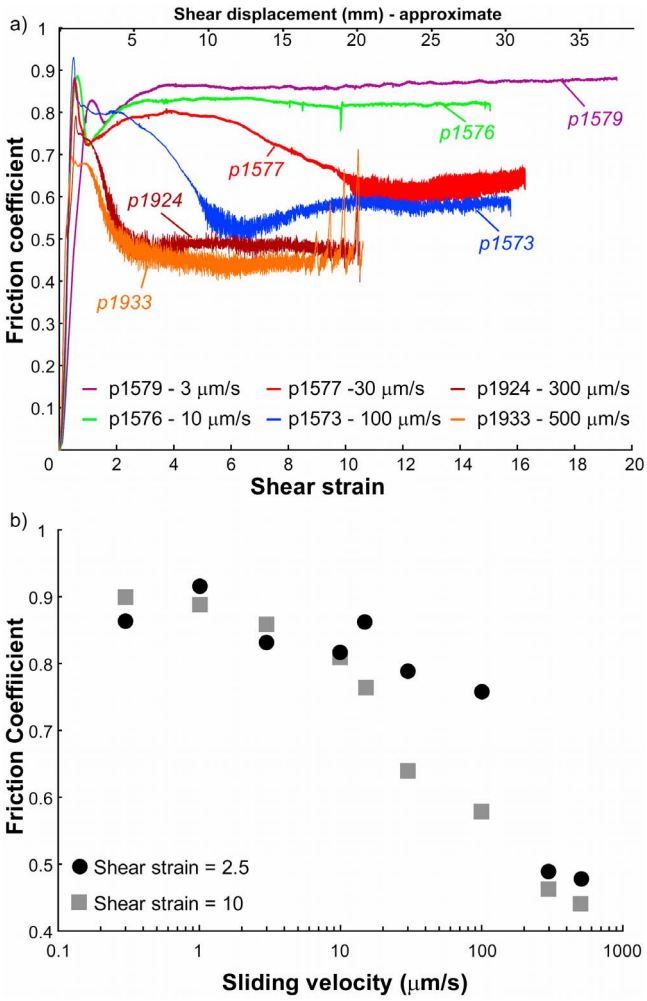

Figure 2. (a) Evolution of friction with shear strain for fault gouges of rock salt (d = 38–106 μm) sheared at constant sliding velocity (as indicated). Note transition from stable sliding to stick slip in the higher velocity runs ($v \geq 30$ μm/s), indicated by variations in friction that resemble noise and begin after weakening. Secondary x-axis shows the approximate displacement corresponding to experiment p1573. Normal stress was 5 MPa in all runs. (b) Steady state friction versus sliding velocity. The average friction values are plotted for experiments with stick-slips. Note that friction decreases above about 30 μm/s.

stepping results from two experiments with grain size of 38–106 μm are shown in Figure 4. This shows that friction evolves upon a velocity step in a typical manner: An up-step in velocity results in an instantaneous increase in friction followed by a gradual drop to a new steady state level and a down-step in velocity leads to an instantaneous decrease in friction followed by a gradual increase in strength. However, in comparison to velocity stepping in "standard" rock friction experiments on granular gouges [e.g., *Tullis*, 1988; *Marone et al.*, 1990; *Beeler et al.*, 1996; *Carpenter et al.*, 2009], the changes in friction we observe are much larger.

[11] We observe qualitatively different behavior for velocity steps performed at low sliding velocities (i.e., <20 μm/s) compared to at high sliding velocities (>20 μm/s). Steps at low velocity show an evolution to a new steady state friction level within the prescribed displacement after the velocity step (1 mm), whereas the steps at high sliding velocity continue to weaken up to the next velocity (down) step. Further, we observe that the velocity steps are not completely reversible (i.e., friction does not return to the prestep level) when the velocity is stepped to a high (>10 μm/s) velocity. Instead, we observe significant strain weakening and reduction in friction (compare friction levels at 10 μm/s in Figure 4 for high strain, p1559 and low strain, p1560). Unstable slip occurs when the velocity is stepped to 100 μm/s after ~1 mm of slip and stays unstable when the velocity is stepped back down to 10 μm/s but becomes stable again when the sliding velocity is 3 μm/s (for p1560).

[12] Figure 5 shows the volumetric behavior of the gouge layers during the velocity steps shown in Figure 4. We show both the raw data and the layer thickness corrected for geometric thinning. These show that the gouge volume (i.e., porosity) decreases when velocity is stepped down and increases when velocity is stepped up. In addition to the

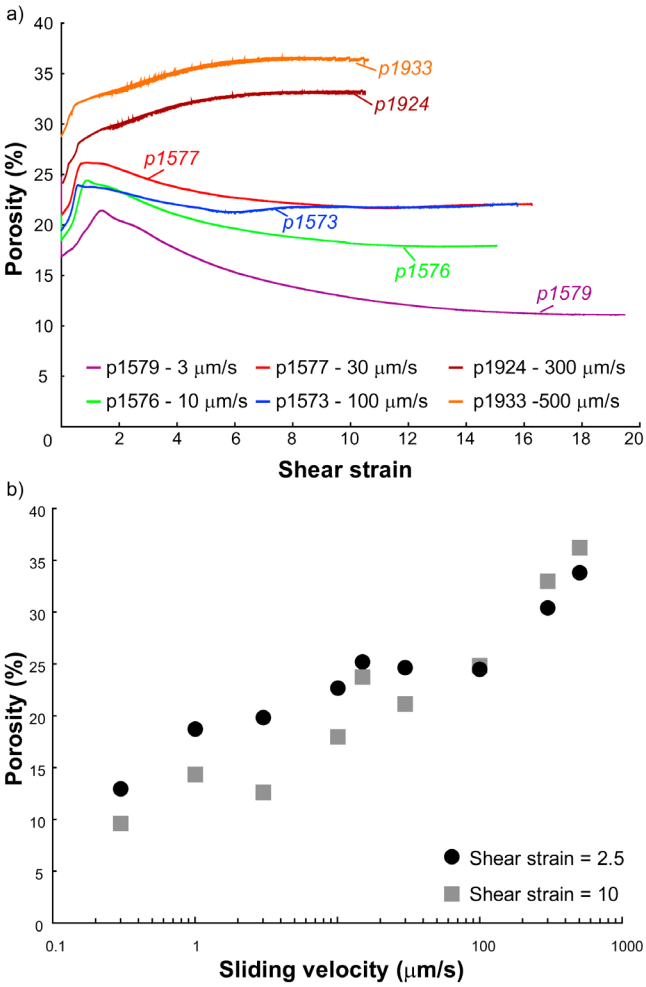

Figure 3. (a) Evolution of porosity with shear strain for fault gouges of rock salt shown in Figure 2a. (grain size 38–106 μm, normal stress 5 MPa). Note that porosity increases upon shear in all cases, but then decreases for the runs with $v \leq 100$ μm/s. (b) Steady state porosity versus sliding velocity. Porosity increases roughly linearly with the log of sliding velocity.

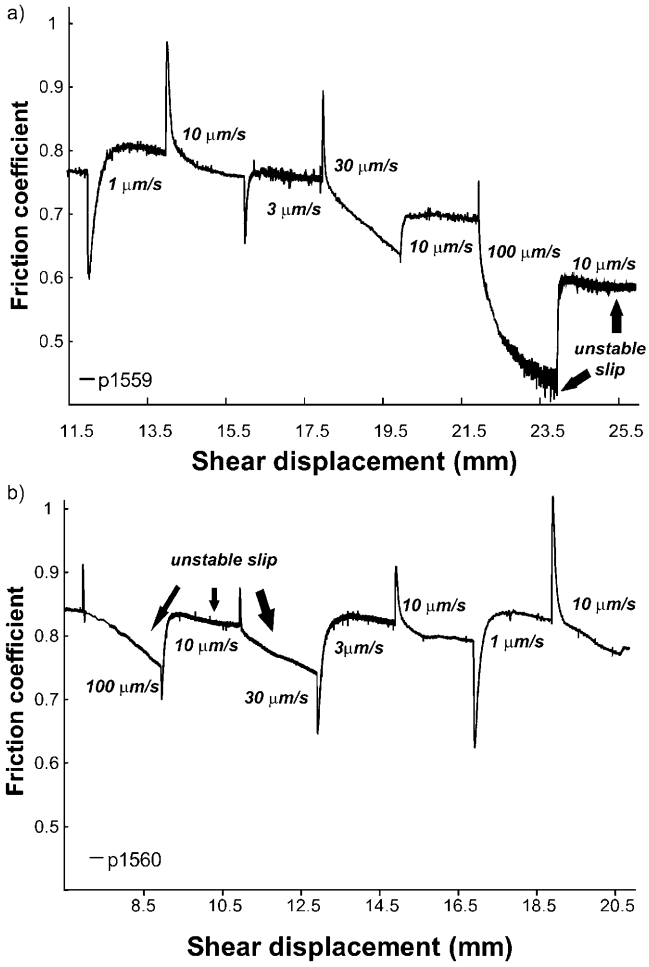

Figure 4. (a) Evolution of friction with shear displacement during the velocity-stepping sequence in experiment p1559 (grain size 38–106 μm, normal stress 5 MPa). Velocity is stepped in the following order: 1–10–3–30–10–100–10 μm/s. (b) Same as (a) but for experiment p1560, in which the velocity-stepping sequence is reversed.

transient changes in layer thickness, there is a long-term dilation (Figure 5a) or compaction trend (Figure 5b), depending on the sequence of velocity steps (low to high or high to low, respectively). That is, the corrected layer thickness at the different 10 μm/s sections increases (Figure 5a) or decreases (Figure 5b) with increasing displacement. This is similar but reverse to the trend in friction as observed in the 10 μm/s sections in Figure 4a but which is not obvious in Figure 4b. The amounts of compaction and dilation seem to correlate with the magnitude of the velocity and to the size of the velocity step.

3.3. Rate and State Frictional Parameters

[13] In the rock friction literature [*Dieterich*, 1979; *Ruina*, 1983] velocity-stepping experiments are usually described using empirical rate-and-state friction (RSF) equations such as

$$\mu = \mu_0 + a\ln\left(\frac{v}{v_0}\right) + b\ln\left(\frac{v_0\theta}{d_c}\right), \quad (1)$$

where μ_0 is the friction coefficient at some reference sliding velocity v_0, v is the sliding velocity, a is the parameter describing the direct effect, b is the parameter describing the evolution effect, d_c is the "critical slip distance," and θ is the state parameter, given by

$$\frac{d\theta}{dt} = 1 - \frac{v\theta}{d_c}\,(\text{Dieterich evolution}) \quad (2a)$$

$$\frac{d\theta}{dt} = \frac{-v\theta}{d_c}\ln\left(\frac{v\theta}{d_c}\right)\,(\text{Ruina evolution}) \quad (2b)$$

The effect of slip velocity on steady state friction is given by the parameter $(a - b)$, which from (1) and (2) is equal to $\Delta\mu/\Delta\ln V$. If the parameter $(a - b)$ is negative, the gouge is velocity weakening and unstable slip is possible (the actual occurrence of unstable slip depends on the stiffness of the system). If the parameter $(a - b)$ is positive, the gouge is velocity strengthening and, in the context of linear stability, only stable, creep-like fault slip is possible.

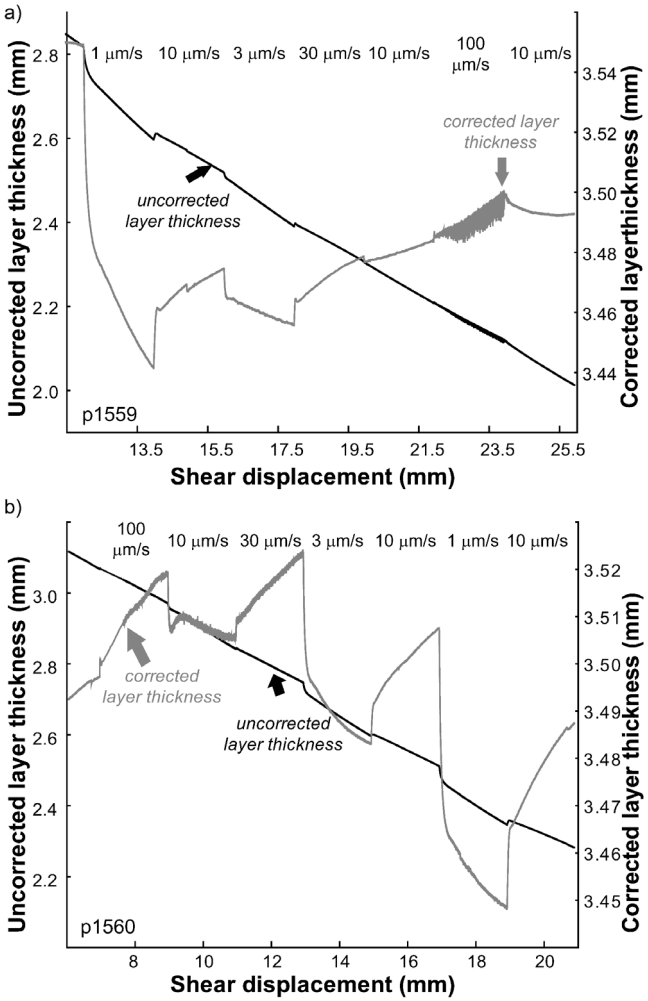

Figure 5. (a) Evolution of layer thickness during the velocity-stepping sequence in experiment p1559. The layer thickness is corrected for geometrical thinning by a linear approximation. (b) Same plot as (a) but for experiment p1560.

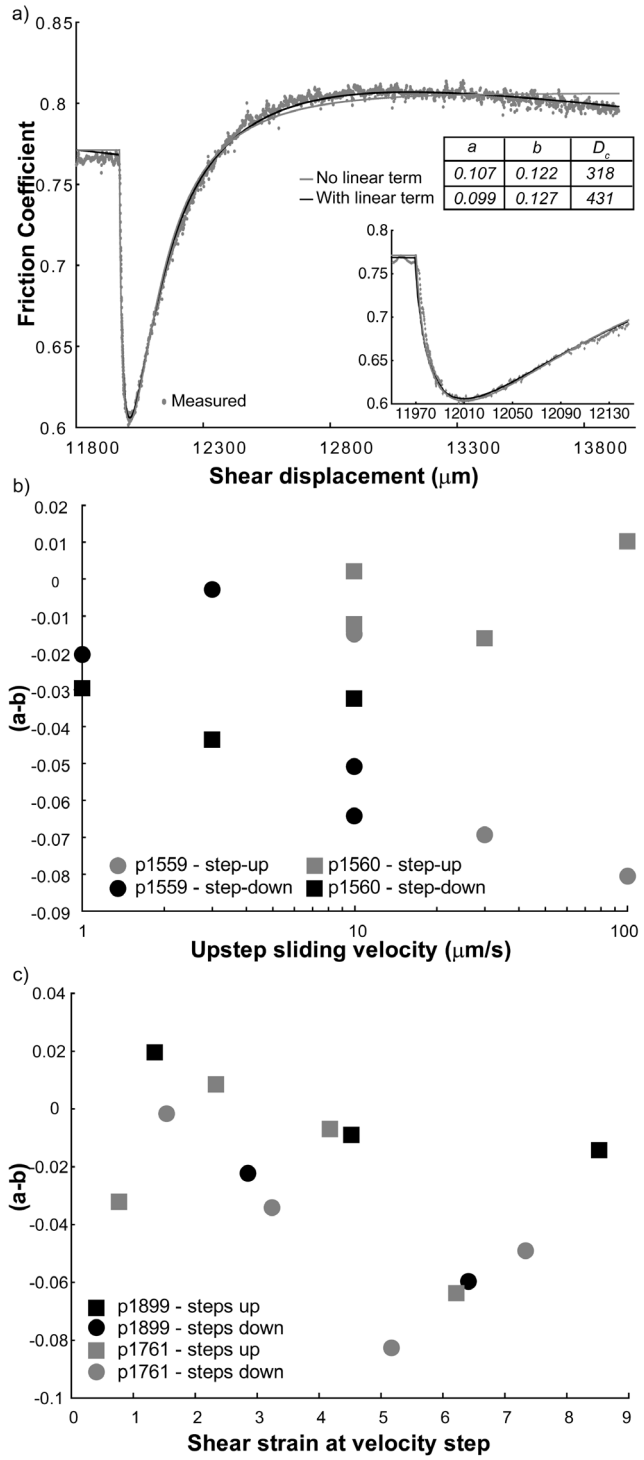

Figure 6. (a) Example of a rate and state friction model inversion showing the experimental data (points) and best-fit model (lines). Velocity step is 10 to 1 μm/s in experiment p1559 (normal stress 5 MPa, grain size 38–106 μm). The fit to the data is improved by adding a linear term to account for strain weakening. (b) Rate and state friction parameter (a–b) versus upstep sliding velocity (experiments p1559 and p1560). A negative value for (a–b) indicates the possibility of unstable slip. (c) Rate and state friction parameter (a–b) versus shear strain for velocity steps from 10 to 100 μm/s and vice versa (experiments p1761 and p1899).

[14] The physical background of the RSF equations is based on the notion that there exists an equilibrium distribution of asperities on mated sliding surfaces shearing at constant sliding velocity. In this model, the direct effect a is interpreted as the effect of loading rate on asperity strength, b is attributed to the change in asperity contact size (strength) due to the change in lifetime of an asperity, and d_c is the distance required to replace the entire population of contacting asperities [e.g., *Tullis and Weeks*, 1987; *Sammis and Steacy*, 1994]. In the case of a granular gouge, the additional effect of dilational work against the normal stress contributes to the friction parameters a and b, but now a and b are interpreted in terms of the formation and failure of grain bridges. The interpretation of the RSF equations in the case of a granular gouge also predicts that the critical slip distance scales with the width of the actively shearing zone [*Marone and Kilgore*, 1993].

[15] We determined the RSF parameters in our velocity stepping experiments (see Table 1) by solving equations (1) and (2), coupled to an equation describing elastic interaction with the testing machine and finding least squares best fits to our data using methods described by *Marone* [1998] and *Blanpied et al.* [1998]. We fit our data in two ways: first by removing displacement-dependent strengthening or weakening and second by applying a correction to the data using a linear term in addition to rate/state friction. In Figure 6a, we show a velocity step (experiment p1559, 10–1 μm/s) with two inversions of the data; one with a linear term and one without, in this case using Dieterich evolution (equation (2a)). The fit to the data is reasonably good for both cases, but the fit is improved by adding the linear term, especially with regard to the evolution of friction. In this case, of a step down in velocity, using a two state variable model does not significantly improve the fit; however, for all up-steps in velocity, a two state variable model provides a much better fit to the data. We have therefore fitted all velocity steps with a one state variable model and a linear term, if required, and otherwise with a two state variable model and a linear term.

[16] In Figure 6b, we show the results for $(a - b)$ as a function of sliding velocity for two experiments (p1559 and p1560). The same slip velocities were used in both experiments, but the velocity step sequence was reversed in experiment p1560, to assess the possible role of slip history. For a single experiment, $(a - b)$ appears to vary systematically with sliding velocity. For p1559, $(a - b)$ decreases (becomes more negative) with increasing sliding velocity, whereas for p1560, it increases with increasing sliding

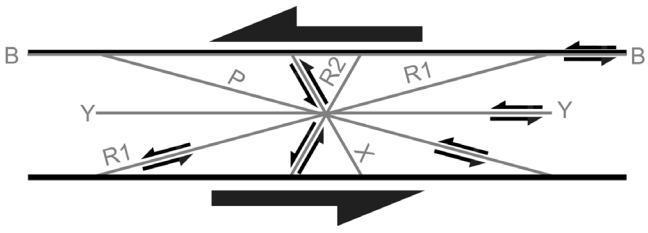

Figure 7. Schematic diagram of a hypothetical fault gouge showing the possible localization phenomena and their nomenclature [after *Logan et al.*, 1992].

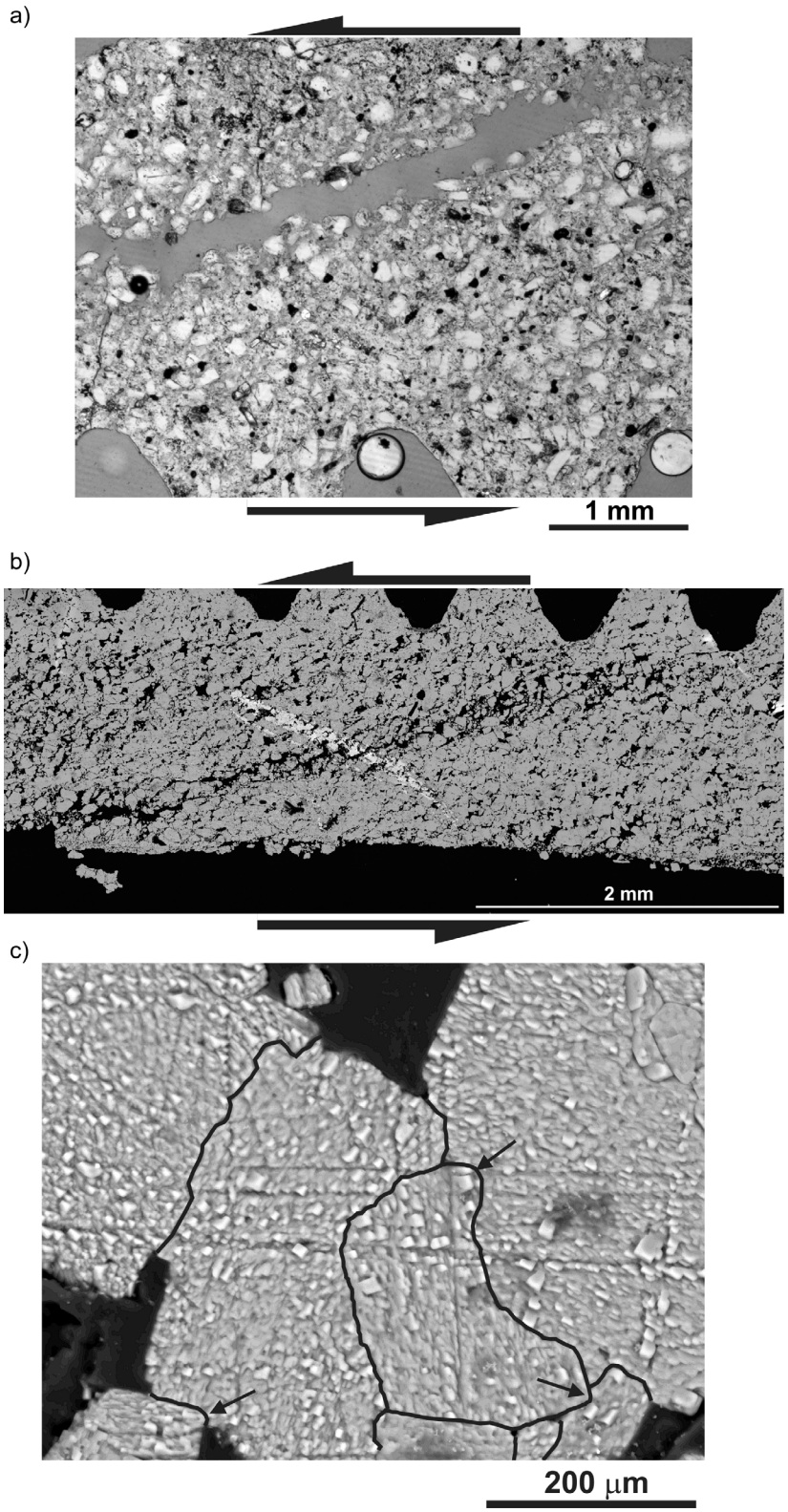

Figure 8. (a) Transmitted light microscope image of sample p1587 (sliding velocity 1 μm/s, normal stress 5 MPa, and shear strain ~20). The microstructure is dominated by dilatant bands in a R1 Riedel orientation. Note that the sample parts along R1 orientation during the process of making thin sections. Dark areas are epoxy resin. (b) Mosaic of Back Scatter Electron Scanning Electron Microscope (BSE-SEM) images of sample p1587. Note R1 Riedel shear indicated by higher porosity and grain breakage. (c) Detailed BSE-SEM image of sample p1587 showing grain-to-grain indentations (white arrows) and long grain boundaries, indicative for the operation of pressure solution.

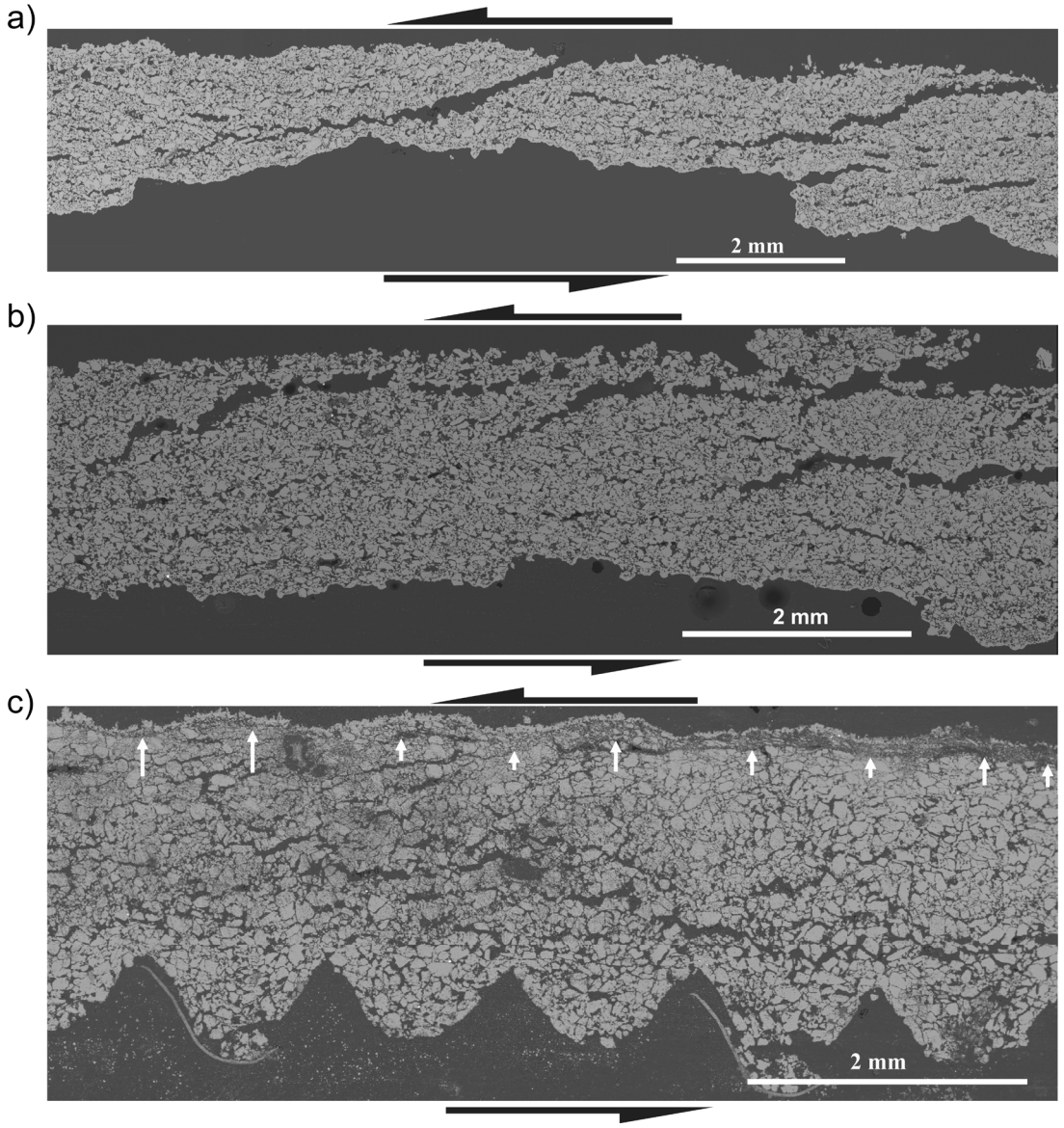

Figure 9. (a) Mosaic of BSE-SEM images of sample p1922 (sliding velocity 100 μm/s, normal stress 5 MPa, and shear strain ~2.7, roughly at the onset point of weakening). The microstructure is dominated by through-going dilatant bands in the R1 Riedel orientation. (b) Mosaic of BSE-SEM images of sample p1993 (sliding velocity 100 μm/s, normal stress 5 MPa, and shear strain ~3.8, roughly at the onset point of unstable, stick-slip sliding). Note that R1 Riedel shear bands are not apparent. Instead, dilatant zones initiating at the upper boundary flatten and terminate in the center of the gouge layer. (c) Mosaic of BSE-SEM images of sample p1573 (sliding velocity 100 μm/s, normal stress 5 MPa, and shear strain ~16). A through-going boundary-parallel (B) shear band (white arrows) is visible on the upper shear zone boundary but not on the lower boundary.

velocity. It is clear that the value of $(a - b)$ depends on the strain at which the velocity steps occur. In fact, the values of $(a - b)$ for the two experiments are almost perfectly mirrored.

[17] To test the dependence of $(a - b)$ on shear strain, we performed experiments in which velocity was stepped between 10 and 100 μm/s repeatedly. The results are summarized in Figure 6c, which demonstrates that there is indeed a large variability in the value of $(a - b)$ with the strain at which the velocity step occurred. On closer inspection of Figure 6c, it can be argued that there is a general decrease in $(a - b)$ with increasing shear strain, i.e., the simulated fault gouge becomes more unstable with increasing shear strain. This is in agreement with the results from the constant sliding velocity experiments at high sliding velocity, where unstable slip eventually occurred after sufficient shear strain had been accumulated (Figure 2a).

3.4. Microstructural Observations

[18] To aid description and interpretation of the microstructures, we show typical gouge fabrics with a (localized) fracture array and their nomenclature in Figure 7 [after

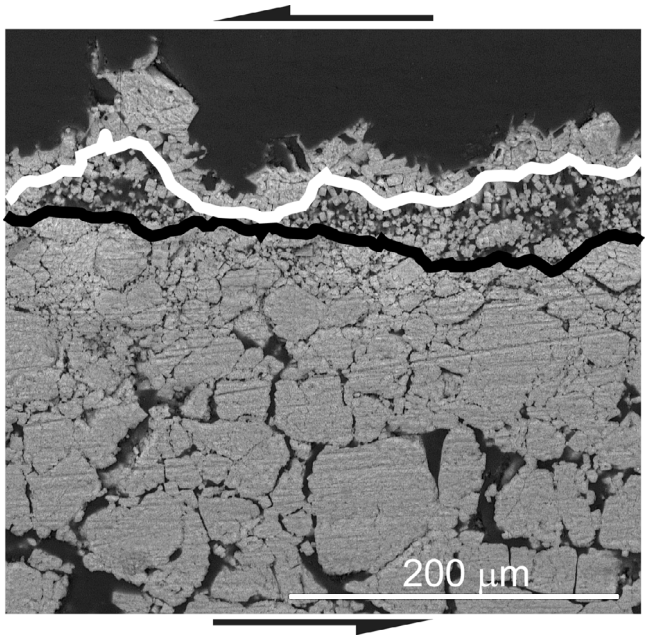

Figure 10. BSE-SEM detail of the boundary-parallel band of Figure 9c, showing alternating zones of low to high to low porosity, roughly indicated by the black and white lines. Very fine grained material is dispersed between the two zones of low(er) porosity. Also note the anastomosing nature of the upper low porosity band.

Logan et al., 1979, 1992]. In Figure 8, we show typical microstructures observed in samples deformed at low sliding velocities (sample p1587, $v = 1$ μm/s). The microstructures are characterized by the presence of dilatant zones in an R_1 Riedel-shear orientation of ~20° to the shear zone boundary (Figure 8). The Riedel shear is characterized by a high local porosity and in some cases the layer separates along this zone during unloading and during the preparation of thin sections. Figure 8b is an enlarged view and shows remnants of the forcing-block teeth (note triangular-shaped features near the top of the image.) The primary R_1 Riedel shear in Figure 8 extends from near the upper right corner to the lower right corner, and additional Riedel shears are also seen near the left side of the image. The boundaries of the Riedel shear zones are irregular with large grains protruding into the zone of finer material that characterizes the shear band. Moreover, porosity decreases strongly with distance into the passive regions and away from the zones of active shear. The bulk of the gouge is characterized by lower porosity and greater interpenetrative grain-to-grain contacts, indicative of the operation of pressure solution, compared to the shear zones (Figure 8c).

[19] Figure 9 shows microstructures obtained from experiments run at high sliding velocity (100 μm/s) and shear strains ranging from 2.7 to 16. Figure 9a shows the microstructure from an experiment that was arrested at the onset of weakening (p1922). Figure 9b shows the microstructure at the initiation of unstable stick slips (p1993), and Figure 9c shows the resulting microstructure after a shear displacement of 35 mm (p1573). It is immediately apparent that the R_1 Riedel, dilatant zones, which are prominent at low sliding velocities (Figure 8), are absent at high sliding velocities (Figures 9b and 9c). The same is true when comparing textures for low (Figure 9a) and high strain (Figures 9b and 9c) at high sliding velocity. The R_1 Riedel shears are not present at high velocity.

[20] One of the dilatant zones visible in Figure 9a has an anastomosing, wavy pattern. Moreover, dispersed throughout the gouge are bands of very high porosity at varying orientations from approximately −15° to +15° (the negative sign indicates a P shear, see Figure 7) that could be remnants of anastomosing dilatant zones. These features are also present in the sample deformed to slightly higher strain (Figure 9b, experiment p1993). Comparing Figures 9a and b, the dilatant zones appear more discontinuous and wavy at higher strain. At the highest strain (Figures 9c and also Figure 10), no distinct dilatant zones in a R_1 orientation are visible. Rather, the gouge appears porous throughout, but porosity is heterogeneous. In addition, a distinct boundary-parallel anastomosing band is apparent. This Y shear band (or B shear) is continuous along the length of the sample and is not present on the lower shear zone boundary, where the imprint of the teeth on the forcing block is preserved.

[21] Figure 10 shows detail of the Y shear, which consists of a high porosity zone sandwiched between two lower porosity zones. The upper zone is characterized by small grain size and low porosity. It does not appear to be completely continuous and its upper boundary includes a relic wavelength that is consistent with the teeth width on the forcing blocks (i.e., see Figures 8b and 9c). In contrast, the lower zone has larger grains (Figure 10), and this low porosity zone is continuous with the top boundary of the higher porosity zone, which is much more linear. Qualitatively, the average grain size increases and the number of small grains decreases with increasing distance from the boundary with the high porosity zone. The grains in the high(er) porosity zone are very small, down to a grain size of ~<1 μm and appear angular to subangular.

4. Mechanisms for Strain Weakening and Velocity Weakening

[22] The mechanical data and microstructural observations for halite gouges deformed at low (<20 μm/s) sliding velocities are very similar to results from previous studies under similar conditions [*Chester and Logan*, 1990; *Bos et al.*, 2000]. In these studies, it was shown that wet halite gouge exhibited stable sliding at low sliding velocities with a friction coefficient of ~0.8–0.9. The mechanical data and microstructural observations led these authors to suggest that shear deformation was distributed and accommodated mainly by cataclasis and faulting of the gouge. Although pressure solution was shown to be active in these gouges, it did not exert influence on the stable sliding strength of the gouges. Instead, pressure solution seems to reduce the gouge porosity during steady state deformation in comparison to gouges where compaction via pressure solution does not occur, whereas shear occurs by pervasive, distributed deformation (cataclasis, grain rotation, and/or grain sliding) accompanied by faulting (through R shears). Our observations of dilatant zones ("faults") in the Riedel orientation and high friction at low sliding velocities suggest that the deformation mechanism was indeed cataclastic flow

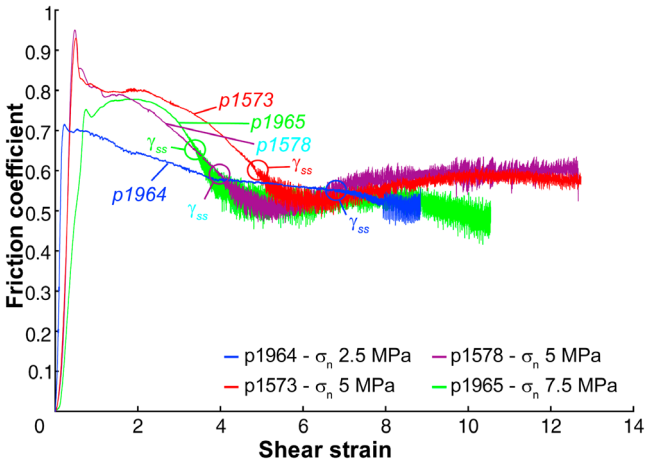

Figure 11. Evolution of friction with shear displacement for four experiments on rock salt gouges (d = 38–106 μm) in the presence of saturated brine at 100 μm/s sliding velocity. Two experiments at 5 MPa normal stress show the high-degree of experimental reproducibility.

accompanied by faulting, with pressure solution acting to reduce the steady state gouge porosity.

[23] Previous studies of simulated fault gouges found that Riedel shears are dominant at shear strains of 1–5 [*Shimamoto and Logan*, 1981; *Marone and Scholz*, 1989; *Logan et al.*, 1992] but due to the kinematic constraint imposed by the boundaries [*Mandl et al.*, 1977], reorientation of the Riedel shears should lead to the development of Y shears after a shear strain of ~5 and even earlier for "soft" materials such as halite and calcite because of the higher initial compaction rates and related thinning of the gouge layer [*Shimamoto and Logan*, 1981]. However, we do not observe Y shears in our low velocity experiments up to a shear strain of 15. In contrast to previous experiments, fluid-assisted compaction (pressure solution) is highly active in our gouges.

[24] We posit that dilation, and localized stress concentrations at grain contacts, in the localized, R_1 zones causes an increased rate of pressure solution driven compaction [*Schutjens*, 1991; *Dewers and Hajash*, 1995; *Niemeijer et al.*, 2002, 2008a]. The increased rate of compaction will tend to destroy any dilatant zones, but at the same time dilation must occur to accommodate the shear deformation. This suggests that dilatant regions are continuously created and destroyed throughout the gouge. In this regime, frictional strength increases with decreasing sliding velocity (e.g., Figure 2), because the steady state porosity is lower (i.e., more net compaction by pressure solution per unit displacement) resulting in more and larger contact areas, which require more stress to break and/or dilate in sliding, which in turn results in a higher overall friction.

[25] In our high sliding velocity experiments, initial shear deformation is apparently accommodated by pervasive and distributed deformation (cataclasis, grain rotation, and/or grain sliding) accompanied by dilation along Riedel shears, similar to the deformation mechanisms at low sliding velocity. Since the sliding velocity is high, the pressure solution compaction rate in the dilatant Riedel shears is not sufficient to re-compact them. Correspondingly, the kinematic constraint of the boundaries leads to a reorientation of the Riedel shears toward Y shears parallel to the shear zone boundary and in extreme cases to P shears (see Figures 9 and 10). This reorientation results in strain weakening. At the same time, grain size reduction by cataclasis leads to the production of fine-grained material that accumulates along the gouge-forcing block interface. Also, the rate of grain fracturing is likely to be higher at the gouge-forcing block interface due to roughness and the sharp contrast in elastic properties.

[26] When sufficient fine-grained material is accumulated to cover the forcing block roughness, a throughgoing weak surface (B shear) is established and shear deformation is fully localized along the boundary shear. Because the boundary shear interface consists of fine-grained fragments, it is prone to healing by solution transfer processes such as pressure solution and possibly Ostwald ripening [*Kay et al.*, 2006], although the time scale seems to be too short for the latter to contribute significantly. The fluid-assisted healing is the most likely cause of the switch to unstable stick slip. At this stage, the overall strength of the gouge is simply controlled by the strength of the boundary-parallel sliding surface. When velocity is decreased while the sample is weakening, the gouge compacts and regains its strength as seen in our velocity-stepping experiments (see Figure 6). The strength is not fully recovered, however, because during the high velocity step the grain size was reduced so that the amount of dilation required in the low velocity step is lower than before, resulting in a slightly lower overall friction.

[27] Recent work on quartz gouges under hydrothermal conditions [*Giger et al.*, 2008] showed strong strain weakening as a result of slip localization at the interface of the gouge and the forcing block. *Giger et al.* [2008] concluded (1) that slip localization and associated weakening occurred due to solution transfer-enhanced gouge densification and strengthening and (2) that these processes were most effective in experiments with higher rates of solution transfer. In contrast, our experiments show the highest friction when the rates of pressure solution are highest (i.e., the lowest sliding velocity) and slip localization along the interface of the gouge and forcing block and associated weakening requires more displacement with increasing rates of pressure solution (i.e., lower sliding velocity, smaller grain size, and higher normal stress). Part of this (apparent) discrepancy might be explained by the rough nature of the forcing blocks used in this study, which prohibits easy forcing block/gouge separation. Moreover, the strain achieved in our study is an order of magnitude higher than that of *Giger et al.* [2008], so that comparison of the results is not straightforward.

[28] In the following, we test our proposed conceptual model for strain weakening, velocity weakening, and stick slip, by varying initial porosity, normal stress, initial grain size, pore fluid, and the roughness of the forcing block. Note, however, that it is not possible to truly isolate the effects of the different parameters, since they influence each other, e.g., a higher normal stress will lead to smaller initial porosities and likely higher rates of grain fracturing and onset of pressure solution.

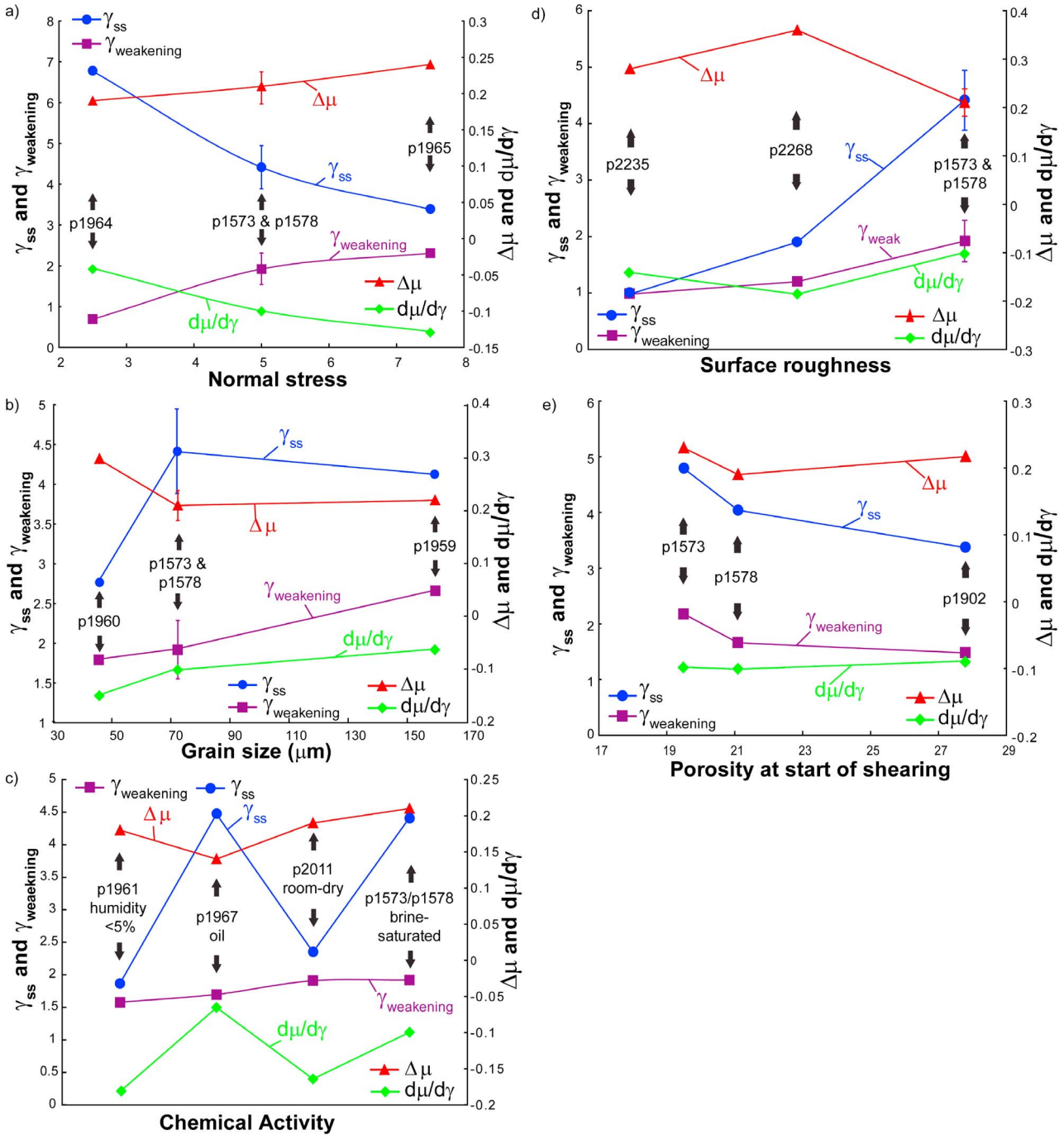

Figure 12. Strain at the onset of weakening ($\gamma_{weakening}$), strain at the initiation of stick-slip (γ_{ss}), amount of weakening ($\Delta\mu$), and weakening rate ($\Delta\mu/\delta\gamma$) versus five variables investigated in this study. Sliding velocity is 100 μm/s in all experiments. (a) Effect of normal stress. The values shown for the experiments at 5 MPa are average values for the two experiments. (b) Effect of initial grain size. Normal stress is 5 MPa and the initial grain size fractions were 38–53, 38–106, and 106–212 μm (see also Table 1). (c) Effect of chemical activity (i.e., different pore fluids: controlled humidity, room-dry or 35% humidity, oil, and saturated brine; see also Table 1). Normal stress is 5 MPa. (d) Effect of forcing block roughness. To vary the roughness of the forcing blocks, we used granite forcing blocks roughened by sandblasting with glass beads (d = 89–149 μm) and sand (d = 200–300 μm) and standard steel forcing blocks with machined grooves. Normal stress is 5 MPa. (e) Effect of initial porosity. Normal stress is 5 MPa.

4.1. Effects of Normal Stress, Initial Grain Size, Fluid Chemistry, Surface Roughness, and Porosity on the Timing of the Onset of Weakening and Stick Slips

[29] In Figure 11, we show the evolution of friction with shear displacement for four experiments at a sliding velocity of 100 μm/s and normal stresses of 2.5, 5, and 7.5 MPa. In the following, we define the amount of weakening, $\Delta\mu_w$, as the difference between the quasi steady state friction after the peak and the average friction level during stick slips. The weakening rate $d\mu/d\gamma$ is the average slope of the linear weakening part of the friction versus shear strain curves, $\gamma_{weakening}$ is the strain at which weakening starts and γ_{ss} is the strain at which stick slips (unstable slip) occur. We investigated the effects of normal stress, initial grain size, fluid chemistry, forcing block roughness, and initial porosity on these parameters.

[30] Although it is not possible to independently vary the different parameters due to the dependence of pressure solution compaction rates on grain size, normal stress and fluid chemistry, some trends emerge from the results shown in Figure 12. First, the strain at which the first stick slips occur decreases as normal stress increases. This strain threshold for stick slip increases with increasing grain size, higher chemical activity of the pore fluid (i.e., with increasing solubility of the salt in the pore fluid), increasing roughness of the forcing blocks, and lower initial porosity (Figures 12a–12e, respectively).

[31] We attribute delayed onset of stick slip to grain size reduction/fragmentation, promoted at higher stress, and to accumulation of fines along the shear zone boundary. With sufficient slip, fine particles infill boundary roughness and provide a throughgoing boundary-parallel slip surface, which subsequently heals during the stick periods by a chemically mediated process (such as pressure solution). The observed trends of γ_{ss} are consistent with this interpretation, since (1) the rate of pressure solution is increased for smaller grains and larger chemical activity, which reduces the production of fines (by cementation), (2) the rate of fracturing increases with normal stress and is reduced for lower initial porosity, and (3) the volume that needs to be fully covered by fines decreases with a lower roughness of the forcing blocks.

[32] We observe that the critical strain for the onset of weakening follows the same trends as the strain at which stick slips occur, although the variation is smaller. The strain for weakening decreases as normal stress increases and increases with increasing grain size, higher chemical activity of the pore fluid, increasing roughness of the forcing blocks, and lower initial porosity. We interpret the onset of weakening as a switch from distributed deformation with faulting along R_1 Riedel shears to localized deformation along boundary-parallel Y and B shears. This switch in deformation style and associated strain weakening has been discussed previously [*Mandl et al.*, 1977; *Weeks and Tullis*, 1985; *Tullis and Weeks*, 1987; *Logan et al.*, 1992; *Marone et al.*, 1992] and attributed to rotation of principal stresses within the gouge layer with accumulating strain. The rotation of the principal stress field leads to the formation of R_1 shears at lower angles to the shear zone boundary, ultimately leading to the formation of boundary-parallel Y and B shears. The timing (i.e., $\gamma_{weakening}$) of the formation of Y and B shears is linked to the distance between the rigid boundaries of the gouge layer that impose a kinematic constraint upon the changing stress field. Therefore, Y shears and B shears develop in a later stage in a thicker gouge layer. In our experiments, the initial thickness of the fault gouge is constant but changes due to initial preshear compaction by pressure solution and subsequent dilation. While a smaller initial porosity would imply a thinner layer and thus an earlier onset of strain weakening, we observe the opposite. We postulate that this is due to the higher dilation rate in samples with a lower initial porosity (analogous to an overcompacted soil), which will actually lead to a thicker gouge layer and thus a later onset of strain weakening. This is also consistent with the effects of normal stress and the chemical activity of the pore fluid on $\gamma_{weakening}$ (Figure 12) but not with the effect of grain size. However, a smaller initial grain size will tend to lower the amount of dilation leading to an overall thinner layer.

[33] The increase in weakening for rougher surfaces is because the bench layer thickness is measured from the peaks of the surface roughness, so that the average initial layer thickness is slightly larger in experiments with rougher forcing blocks. The trends for the total amount of weakening ($\Delta\mu$) and the weakening rate ($d\mu/d\gamma$) show considerable variation but in general roughly follow the trends described for $\gamma_{weakening}$ and γ_{ss}, respectively. The amount of weakening seems to be affected mostly by the initial porosity and subsequent dilation, whereas the weakening rate is mostly controlled by the competition between grain size reduction and chemically aided healing or cementation.

4.2. A Note on Slip Weakening and Critical Slip Distance

[34] In recent experimental studies of high velocity friction, investigators have reported values for the slip weakening distance (confusingly referred to as D_c), which have been compared to seismological estimates [*Hirose and Shimamoto*, 2007; *Mizoguchi et al.*, 2007; *Cocco et al.*, 2009; *Marone et al.*, 2009; *Sone and Shimamoto*, 2009]. This slip weakening distance (or the breakdown distance) is defined as the slip distance from peak friction to some residual "steady state" friction value and is determined in experiments by an exponential fit to the data. In contrast, the critical slip distance d_c [*Marone and Kilgore*, 1993 and equations 1 and 2] or L [*Scholz*, 1988] is the characteristic distance of the exponential decay or increase following an immediate friction change after a step in sliding velocity (up or down). Strictly speaking, one can only report critical slip distances from velocity-stepping experiments, since d_c (or L) is defined according to equations (1) and (2).

[35] Moreover, the original definition of the critical slip distance d_c by *Ruina* [1983] is for two contacts sliding over each other. It has been shown that the effective critical slip distance, d_{cb} (where the b indicates "bulk") for gouges is dependent on gouge thickness, the degree of localization of deformation, and the grain size. We will use d_{cb} for the effective critical slip distance and, to avoid confusion, propose to use d_w for the slip weakening distance obtained from an exponential fit of experimental data at constant sliding velocity.

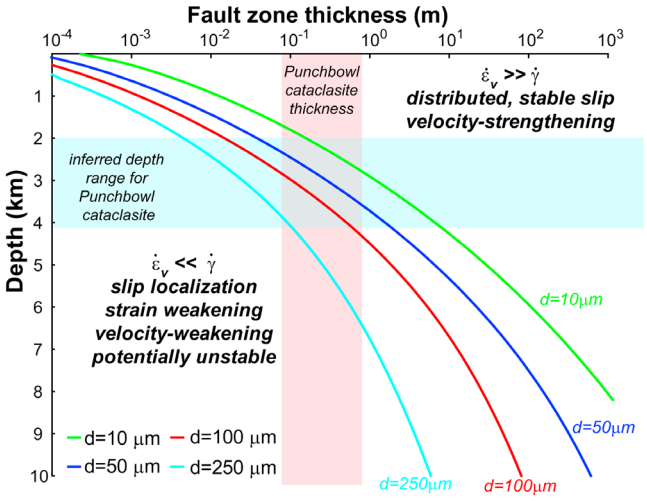

Figure 13. Plot showing the fault zone thicknesses as a function of depth predicted from a comparison of volumetric compaction rate (through pressure solution) and shear strain rate. Also indicated are the inferred depth range and measured thickness range for a quartz-rich cataclasite of the Punchbowl fault [*Chester and Chester*, 1998]. The kinetic parameters used for the calculation of the volumetric compaction rate were the same as those used by *Niemeijer and Spiers* [2007].

[36] In our experiments, we have the possibility to compare the two parameters, since we have both velocity-stepping and constant velocity experiments. From Figure 2, we can estimate the slip weakening distance d_w to be around ~5 mm at a sliding velocity of 100 μm/s. In contrast to high velocity experiments [e.g., *Sone and Shimamoto*, 2009], the slip weakening distance decreases with increasing sliding velocity in our experiments, down to ~2 mm at 500 μm/s. In comparison, the critical slip distance for a velocity step from 10 to 100 μm/s as determined by our calculations is 160 μm and 4100 μm in experiments p1559 and p1560, respectively. A similar decrease in d_{cb} with increasing strain is seen in experiments p1761 and p1899, in which velocity was cycled between 10 and 100 μm/s and d_{cb} decreases from 25,000 μm initially, down to 135 μm at the end of the experiment. This decrease in critical slip distance with increasing shear strain has been observed in other experimental studies [e.g., *Marone and Kilgore*, 1993] and can be explained by increased localization of deformation. At the same time, the slip weakening distance d_w seems to be affected by the initial state of fault gouge. With only a slight change in initial porosity from 28% to 20%, the observed slip weakening distance increases from ~3 to ~5 mm. In summary, both the values of the (effective or bulk) critical slip distance d_{cb} and the slip weakening distance d_w are strongly influenced by the microstructural evolution of the gouge (i.e., porosity, degree of localization, grain size, and thickness) and its slip history. To extrapolate these values to natural fault zones, an appropriate scaling law has to be applied [see, e.g., *Marone et al.*, 2009, and references therein], and thus, a direct comparison between laboratory-derived and seismologically obtained values is not straightforward.

4.3. Implications for Natural Fault Zones

[37] To extrapolate our experimental results to natural fault zones under hydrothermal conditions and crustal stress levels, we have to make a number of assumptions. First, we assume that pressure solution operates in natural fault rocks under hydrothermal conditions at similar rates as in our experiments. This seems to be a reasonable assumption since pressure solution features have been observed in a number of natural fault zones [e.g., *Imber et al.*, 1997; *Stewart et al.*, 2000; *Holdsworth*, 2004; *Jefferies et al.*, 2006], and experimental and modeling studies have demonstrated pressure solution in quartzose materials under hydrothermal conditions [e.g., *Cox and Paterson*, 1991; *Dewers and Hajash*, 1995; *Karner et al.*, 1997; *Renard et al.*, 2000; *Gundersen et al.*, 2002; *Niemeijer and Spiers*, 2002; *Niemeijer et al.*, 2002; *Bernabé and Evans*, 2007]. Furthermore, we have to assume that grain size reduction and fragmentation during shear occurs in natural fault zones at comparable rates. The strength and hardness of quartz is quite different from that of halite (hardness 7 versus 2.5 and compressive strength 100 versus ~40 MPa), but since our experiments were performed under a low normal stress of 5 MPa compared to the conditions in natural fault zones in the upper to middle crust (3–10 km, stresses of ~75–250 MPa), the laboratory stresses might represent a good analogue for natural in situ stresses. The observation of fine-grained material in thin slipping zones in exhumed fault zones in nature further suggests that grain size reduction and fragmentation is an active mechanism during various stages of fault zone development. A third assumption in extrapolating our experiments to natural conditions lies in the simplicity of the experimental geometry compared to the complexity of natural fault zones, which contain kinks, bends, and varying wall rock composition and roughness. These factors are difficult to reproduce in the laboratory, but by varying the forcing block roughness, we have made a first attempt to investigate the effects of these. In summary, we believe it is valid and appropriate to make a first order attempt to extrapolate our results to natural fault rocks under hydrothermal conditions to put forward some implications of this work for natural fault rock mechanics.

[38] The results of our experiments suggest that the interplay of grain size reduction and/or fragmentation with the operation of pressure solution can lead to a complex evolution of the strength of a fault zone. A variation in loading rate of only 2 orders of magnitude could result in a strength contrast of up to 0.4 units in friction coefficient. Furthermore, at the higher end of these loading rates, shear strain, and wall rock roughness become an important factor in controlling the mode of sliding.

[39] The shear strain rate at which the transition between velocity (and strain) strengthening and weakening occurs may be approximated from the sliding velocity of ~15 μm/s and a gouge thickness of ~3 mm as ~5 × 10^{-3} s^{-1}. At the same time, the compaction rate via pressure solution can be calculated using a simple model for a granular aggregate of mono-sized spheres in a simple cubic packing [see, e.g., *Spiers et al.*, 1990; *Niemeijer et al.*, 2002, 2008a, 2009]. We use a model with the rate of pressure solution being controlled by diffusion and use 10^{-11} m^2/s for the diffusion coefficient and 100 nm for the average fluid film thickness

[*de Meer et al.*, 2002, 2005; *van Noort et al.*, 2006] and calculate a compaction rate of 5×10^{-4} s^{-1} for a porosity of 25% and an average grain size of 72 μm. However, when we use a grain size of ~30 μm that is more representative of the average grain size observed after the experiment, we get a rate of 7×10^{-3} s^{-1} that increases to 6×10^{-2} s^{-1} when we use a grain size of 15 μm. It is interesting to note that these compaction rates are very close to the overall shear strain rate of 5×10^{-3}. Combined with the observation of fine grains of 10–20 μm in the boundary parallel shear zone, we propose that pressure solution may act to strengthen fault gouges to Byerlee friction values of >0.6 when the compaction rate exceeds the shear strain rate. When the shear strain rate exceeds the compaction rate, the gouge deformation is dominated by dilation and grain size reduction that produces fine-grained material and shear localization that in turn can lead to unstable slip. Although we are not aware of any microstructural evidence of exhumed fault zones showing evidence for this type of pressure solution rate-controlled transition, based on our experimental results and the notion that pressure solution should be widespread in the upper crust [e.g., *Rutter*, 1983], we infer that a similar transition might occur in natural fault rocks as well. Therefore, in Figure 13, we show a depth profile for a strike-slip fault that shows the transition between stable velocity and strain strengthening slip and unstable velocity and strain weakening slip based on a comparison of calculated pressure solution compaction rates using the appropriate kinetics for quartz [e.g., *Niemeijer and Spiers*, 2007] and shear strain rates for faults of different thicknesses and grain sizes. For a grain size of 10 μm, we estimate the depth of transition from stable to potentially unstable slip to be between 2 and 3 km for fault zones between 0.1 and 1 m thick. The depth range for the occurrence of shear in the exhumed Punchbowl Fault in California, which is part of San Andreas system, was estimated to be 2–4 km [*Chester and Chester*, 1998]. *Chester and Chester* [1998] have shown that most of the slip along the Punchbowl Fault was accommodated in two distinct ultracataclasite layers with a thickness varying between 0.15 and 0.55 m. Further localization occurred along a single, continuous, nearly planar, prominent fracture surface (pfs), contacting the ultracataclasite. The grain size within the ultracataclasites was measured to be <10 μm. The occurrence of the ultracataclasite in combination with the pfs is very similar to the microstructures found at high strain in our experiments, with a thin continuous boundary-parallel shear surface (experimental pfs). It is surprising that using a simple model, we predict a depth range and fault zone thickness for the transition from distributed to localized slip that is roughly consistent with field observations.

5. Conclusions

[40] We performed frictional sliding experiments on simulated fault gouges of rock salt in the presence of saturated brine under a variety of conditions of normal stress and sliding velocity to investigate the effects of the operation of chemically assisted fluid-rock processes on the mechanical behavior of faults. The mechanical data and microstructural observations indicate that

[41] 1. Gouges of rock salt exhibit a transition from velocity-strengthening to strongly velocity-weakening behavior at sliding velocities of ~15–20 μm/s.

[42] 2. The values of the rate-and-state friction parameter ($a - b$) are an order of magnitude larger than those determined in experiments under conditions where solution-transfer processes do not operate at a significant rate.

[43] 3. Strong strain weakening in fault gouges of rock salt can be associated to a rotation of the principal stress field within the fault gouge, ultimately leading to the development of Y and B shears.

[44] 4. The production of fine-grained material and subsequent accumulation of this material along the gouge-forcing block interface ultimately results in the formation of a throughgoing boundary-parallel slip surface that fails in an unstable manner. We infer that healing during the stick phase of the stick-slip cycles occurs by solution-transfer processes.

[45] 5. The onset of strain weakening and the occurrence of stick slips are controlled by the interplay of chemical strengthening through healing and cementation of fine particles and the reduction of porosity and mechanical weakening through grain size reduction and the rotation of the internal principal stress field.

[46] **Acknowledgments.** The authors like to thank the associate editor, Silvio Giger, and an anonymous reviewer for their comments that helped to improve this manuscript. The support of the Netherland Organisation of Scientific Research (N.W.O.) under Rubicon grant 825.06.003, the U.S. National Science Foundation under grants OCE-0648331 and EAR-0510182 and the European Research Council under starting grant 205175, USEMS project (P.I. Giulio di Toro), is gratefully acknowledged.

References

Beeler, N. M., T. E. Tullis, M. L. Blanpied, and J. D. Weeks (1996), Frictional behavior of large displacement experimental faults, *J. Geophys. Res.*, *101*(B4), 8697–8715, doi:10.1029/96JB00411.

Bernabé, Y., and B. Evans (2007), Numerical modeling of pressure solution deformation at axisymmetric asperities under normal load, *Geol. Soc. London, Spec. Publ.*, *284*, 185–205, doi:10.1144/SP1284.1113, 1185-1205.

Blanpied, M. L., D. A. Lockner, and J. D. Byerlee (1995), Frictional slip of granite at hydrothermal conditions, *J. Geophys. Res.*, *100*(B7), 13,045–13,064, doi:10.1029/95JB00862.

Bos, B., C. J. Peach, and C. J. Spiers (2000), Slip behavior of simulated gouge-bearing faults under conditions favoring pressure solution, *J. Geophys. Res.*, *105*(B7), 16,669–16,718, doi:10.1029/2000JB900089.

Bos, B., and C. J. Spiers (2002a), Frictional-viscous flow of phyllosilicate-bearing fault rock: Microphysical model and implications for crustal strength profiles, *J. Geophys. Res.*, *107*(B2), 2028, doi:10.1029/2001JB000301.

Bos, B., and C. J. Spiers (2002b), Fluid-assisted healing processes in gouge-bearing faults: Insights from experiments on a rock analogue system, *Pure Appl. Geophys.*, *159*(11–12), 2537–2566.

Byerlee, J. (1994), The role of water in the evolution of large crustal faults such as the San Andreas in California, in *The mechanical involvement of fluids in faulting*, edited by S. Hickman et al., pp. 254–261, U.S. Geol. Surv. Open File Rep., Menlo Park, Calif.

Carpenter, B. M., C. Marone, and D. M. Saffer (2009), Frictional behavior of materials in the 3-D SAFOD volume, *Geophys. Res. Lett.*, *36*, L05302, doi:10.1029/2008GL036660.

Chester, F. M., and J. M. Logan (1990), Frictional faulting in polycrystalline halite: Correlation of microstructure, mechanisms of slip, and constitutive behaviour, in *The brittle-ductile transition in rocks: the Heard volume*, edited by A. G. Duba et al., *Am. Geophys. Union Geophys. Monogr.*, 56, 49–65.

Chester, F. M., and N. G. Higgs (1992), Multimechanism friction constitutive model for ultrafine quartz gouge at hypocentral conditions, *J. Geophys. Res.*, *97*(B2), 1859–1870, doi:10.1029/91JB02349.

Chester, F. M. (1994), Effects of temperature on friction: Constitutive equations and experiments with quartz gouge, *J. Geophys. Res.*, *99*(B4), 7247–7261, doi:10.1029/93JB03110.

Chester, F. M. (1995), A rheologic model for wet crust applied to strike-slip faults, *J. Geophys. Res.*, *100*(B7), 13,033–13,044, doi:10.1029/95JB00313.

Chester, F. M., and J. S. Chester (1998), Ultracataclasite structure and friction processes of the Punchbowl Fault, San Andreas system, California, *Tectonophysics*, *295*(1–2), 199–221.

Cocco, M., C. Marone, E. Tinti, and A. Piatanesi (2009), Scaling of slip weakening distance with final slip during dynamic earthquake rupture, in *Fault-zone Properties and Earthquake Rupture Dynamics*, edited by E. Fukuyama, Elsevier.

Cox, S. F., and M. S. Paterson (1991), Experimental dissolution-precipitation creep in quartz aggregates at high temperatures, *Geophys. Res. Lett.*, *18*(8), 1401–1404, doi:10.1029/91GL01802.

Cox, S. F. (1994), Low friction during sliding on simulated faults in porous quartz sandstone at hydrothermal conditions, in *The mechanical involvement of fluids in faulting*, edited by S. Hickman et al., pp. 501–508, U.S. Geol. Surv. Open File Rep., Menlo Park, Calif.

de Meer, S., C. J. Spiers, C. J. Peach, and T. Watanabe (2002), Diffusive properties of fluid-filled grain boundaries measured electrically during active pressure solution, *Earth Planet. Sci. Lett.*, *200*(1–2), 147–157.

de Meer, S., C. J. Spiers, and S. Nakashima (2005), Structure and diffusive properties of fluid-filled grain boundaries: An in-situ study using infrared (micro) spectroscopy, *Earth Planet. Sci. Lett.*, *232*, 403–414.

Dewers, T. A., and A. Hajash (1995), Rate laws for water-assisted compaction and stress-induced water- rock interaction in sandstones, *J. Geophys. Res.*, *100*(B7), 13,093–13,112, doi:10.1029/95JB00912.

Dieterich, J. H. (1979), Modeling of rock friction 1. Experimental results and constitutive equations, *J. Geophys. Res.*, *84*(B5), 2162–2168, doi:10.1029/JB084iB05p02161.

Faulkner, D. R., and E. H. Rutter (2001), Can the maintenance of overpressured fluids in large strike-slip fault zones explain their apparent weakness?, *Geology*, *29*(6), 503–506.

Giger, S. B., E. Tenthorey, S. F. Cox, and J. D. Fitz Gerarld (2007), Permeability evolution in quartz fault gouges under hydrothermal conditions, *J. Geophys. Res.*, *112*, B07202, doi:10.1029/2006JB004828.

Giger, S. B., S. F. Cox, and E. Tenthorey (2008), Slip localization and fault weakening as a consequence of fault gouge strengthening—Insights from laboratory experiments, *Earth Planet. Sci. Lett.*, *276*, 73–84.

Gundersen, E., D. K. Dysthe, F. Renard, K. Bjørlykke, and B. Jamtveit (2002), Numerical modelling of pressure solution in sandstone, rate-limiting processes and the effect of clays, in *Deformation Mechanisms, Rheology and Tectonics*, edited by S. De Meer et al., *Geol. Soc. London*, 200, 41–60.

Hickman, S. H., and B. Evans (1995), Kinetics of pressure solution at halite-silica interfaces and intergranular clay films, *J. Geophys. Res.*, *100*(B7), 13,113–13,132, doi:10.1029/95JB00911.

Hirose, T., and T. Shimamoto (2007), Slip-weakening distance of faults during frictional melting as inferred from experimental and natural pseudotachylytes, *Bull. Seismol. Soc. Am.*, *95*, 1666–1673.

Holdsworth, R. E. (2004), Weak faults—Rotten cores, *Science*, *303*, 181–182.

Imber, J., R. E. Holdsworth, C. A. Butler, and G. Lloyd (1997), Fault-zone weakening processes along the reactivated Outer Hebrides Fault Zone, Scotland, *J. Geol. Soc. London*, *154*, 105–109.

Jefferies, S. P., R. E. Holdsworth, C. A. J. Wibberley, T. Shimamoto, C. J. Spiers, A. R. Niemeijer, and G. E. Lloyd (2006), The nature and importance of phyllonite development in crustal-scale fault cores: An example from the Median Tectonic Line, Japan, *J. Struct. Geol.*, *28*, 220–235.

Kanagawa, K., S. F. Cox, and S. Zhang (2000), Effects of dissolution-precipitation processes on the strength and mechanical behavior of quartz gouge at high-temperature hydrothermal conditions, *J. Geophys. Res.*, *105*(B5), 11,115–11,126, doi:10.1029/2000JB900038.

Karner, S. L., C. Marone, and B. Evans (1997), Laboratory study of fault healing and lithification in simulated fault gouge under hydrothermal conditions, *Tectonophysics*, *277*, 41–55.

Kay, M. A., I. G. Main, S. C. Elphick, and B. T. Ngwenya (2006), Fault gouge diagenesis at shallow burial depth: Solution-precipitation reactions in well-sorted and poorly sorted powders of crushed sandstone, *Earth Planet. Sci. Lett.*, *243*, 607–614.

Logan, J. M., M. Friedman, N. Higgs, C. Dengo, and T. Shimamoto (1979), Experimental studies of simulated gouge and their application to studies of natural fault zones, in *Proc. Conf. VIIII Analysis of Actual Fault Zones in Bedrock*, *U.S. Geol. Surv. Open File Rep.*, 305–343.

Logan, J. M., C. A. Dengo, N. G. Higgs, and Z. Z. Wang (1992), Fabrics of Experimental fault zones: Their development and relationship to mechanical behavior, in *Fault Mechanics and Transport Properties of Rocks*, edited by B. Evans and T.-F. Wong, pp. 33–67, Academic Press, London, U. K.

Mandl, G., L. N. J. de Jong, and A. Maltha (1977), Shear zones in granular material, *Rock Mech.*, *9*, 95–144.

Marone, C., and C. H. Scholz (1989), Particle-size distribution and microstructures within simulated fault gouge, *J. Struct. Geol.*, *11*(7), 799–814.

Marone, C., B. Raleigh, and C. H. Scholz (1990), Frictional behavior and constitutive modeling of simulated fault gouge, *J. Geophys. Res.*, *95*(B5), 7007–7025, doi:10.1029/JB095iB05p07007.

Marone, C., B. E. Hobbs, and A. Ord (1992), Coulomb constitutive laws for friction: Contrasts in behavior for distributed and localized shear, *Pure Appl. Geophys.*, *139*, 195–214.

Marone, C., and B. Kilgore (1993), Scaling of the critical slip distance for seismic faulting with shear strain in fault zones, *Nature*, *362*, 618–621.

Marone, C. (1998), Laboratory-derived friction laws and their application to seismic faulting, *Ann. Rev. Earth Planet. Sci.*, *26*, 643–696.

Marone, C., M. Cocco, E. Richardson, and E. Tinti (2009), The critical slip distance for seismic and aseismic fault zones finite width, in *Fault-zone Properties and Earthquake Rupture Dynamics*, edited by E. Fukuyama, pp. 135–162, Elsevier.

Mizoguchi, K., T. Hirose, T. Shimamoto, and E. Fukuyama (2007), Reconstruction of seismic faulting by high-velocity friction experiments: An example of the 1995 Kobe earthquake, *Geophys. Res. Lett.*, *34*, L01308, doi:10.1029/2006GL027931.

Niemeijer, A., C. Marone, and D. Elsworth (2008a), Healing of simulated fault gouges aided by pressure solution: Results from rock analogue experiments, *J. Geophys. Res.*, *113*, B04204, doi:10.1029/2007JB005376.

Niemeijer, A. R., C. J. Spiers, and C. J. Peach (2008b), Frictional behaviour of simulated quartz fault gouges under hydrothermal conditions: Results from ultra-high strain rotary shear experiments, *Tectonophysics*, *460*, 288–303.

Niemeijer, A., D. Elsworth, and C. Marone (2009), Significant effect of grain size distribution on compaction rates in granular aggregates, *Earth Planet. Sci. Lett.*, *284*, 386–391, doi.10.1016/j.epsl.2009.1004.1041.

Niemeijer, A. R., and C. J. Spiers (2002), Compaction creep of quartz-muscovite mixtures at 500°C: Preliminary results on the influence of muscovite on pressure solution, in *Deformation Mechanisms, Rheology and Tectonics*, edited by S. De Meer et al., *Geol. Soc. London*, 200, 61–71.

Niemeijer, A. R., C. J. Spiers, and B. Bos (2002), Compaction creep of quartz sand at 400°C–600°C: Experimental evidence for dissolution-controlled pressure solution, *Earth Planet. Sci. Lett.*, *195*(3–4), 261–275.

Niemeijer, A. R., and C. J. Spiers (2005), Influence of phyllosilicates on fault strength in the brittle-ductile transition: Insights from rock analogue experiments, in *High-Strain Zones: Structure and Physical Properties*, edited by D. Bruhn and L. Burlini, *Geol. Soc. London*, 245, 303–327.

Niemeijer, A. R., and C. J. Spiers (2006), Velocity dependence of strength and healing behaviour in simulated phyllosilicate-bearing fault gouge, *Tectonophysics*, *427*, 231–253.

Niemeijer, A. R., and C. J. Spiers (2007), A microphysical model for strong velocity weakening in phyllosilicate-bearing fault gouges, *J. Geophys. Res.*, *112*, B10405, doi:10.1029/2007JB005008.

Renard, F., J.-P. Gratier, and B. Jamtveit (2000), Kinetics of crack-sealing, intergranular pressure solution, and compaction around active faults, *J. Struct. Geol.*, *22*(10), 1395–1407.

Rice, J. R. (1992), Fault stress strates, pore pressure distributions, and the weakness of the San Andreas fault, in *Earthquake mechanics and transport properties of rocks*, edited by B. Evans and T.-F. Wong, pp. 475–503, Academic Press, London.

Ruina, A. (1983), Slip instability and state variable friction laws, *J. Geophys. Res.*, *88*(B12), 10,359–10,370, doi:10.1029/JB088iB12p10359.

Rutter, E. H., and D. H. Mainprice (1979), On the possibility of slow fault slip controlled by a diffusive mass transfer process, *Gerlands Beitr. Geophysik*, *88*(2), 154–162.

Rutter, E. H. (1983), Pressure solution in nature, theory and experiment, *J. Geol. Soc. London*, *140*, 725–740.

Sammis, C. G., and S. J. Steacy (1994), The micromechanics of friction in a granular layer, *Pure Appl. Geophys.*, *142*(3/4), 778–794.

Scholz, C. H. (1988), The critical slip distance for seismic faulting, *Nature*, *336*, 761–763.

Schutjens, P. M. T. M. (1991), Experimental compaction of quartz sand at low effective stress and temperature conditions, *J. Geol. Soc. London*, *148*, 527–539.

Schutjens, P. M. T. M., and C. J. Spiers (1999), Intergranular pressure solution in NaCl: Grain-to-grain contact experiments under the optical microscope, *Oil Gas Sci. Tech.*, *54*, 729–750.

Scott, D. R., C. J. Marone, and C. G. Sammis (1994), The apparent friction of granular fault gouge in sheared layers, *J. Geophys. Res.*, *99*(B4), 7231–7246, doi:10.1029/93JB03361.

Shimamoto, T., and J. M. Logan (1981), Effects of simulated fault gouge on the sliding behavior of Tennessee sandstone: Nonclay gouges, *J. Geophys. Res.*, *86*, 2902–2914, doi:10.1029/JB086iB04p02902.

Sibson, R. H. (1973), Interactions between temperature and pore-fluid pressure during earthquake faulting and a mechanism for partial or total stress relief, *Nature*, *243*, 66–68.

Sibson, R. H. (2001), Seismogenic framework for hydrothermal transport and ore deposition, *Rev. Econ. Geol.*, *14*, 25–50.

Sone, H., and T. Shimamoto (2009), Frictional resistance of faults during accelerating and decelerating earthquake slip, *Nat. Geosci.*, *2*, 705–708, doi:10.1038/NGEO1637.

Spiers, C. J., and P. M. T. M. Schutjens (1990), Densification of crystalline aggregates by fluid phase diffusional creep, in *Deformation Processes in Minerals, Ceramics and Rocks*, edited by D. J. Barber and P. G. Meredith, pp. 334–353, Unwin Hyman, London.

Spiers, C. J., P. M. T. M. Schutjens, R. H. Brzesowsky, C. J. Peach, J. L. Liezenberg, and H. J. Zwart (1990), Experimental determination of constitutive parameters governing creep of rock salt by pressure solution, in *Deformation mechanisms, rheology and tectonics*, *Geol. Soc. London*, 54, 215–227.

Spiers, C. J., S. De Meer, A. R. Niemeijer, and X. Zhang (2004), Kinetics of rock deformation by pressure solution and the role of thin aqueous films, in *Physicochemistry of water in geological and biological systems*, edited by S. Nakashima et al., pp. 129–158, Univ. Acad. Press, Inc., Tokyo, Japan.

Stewart, M., R. E. Holdsworth, and R. A. Strachan (2000), Deformation processes and weakening mechanisms within the frictional-viscous transition zone of major crustal-scale faults: Insights from the Great Glen Fault Zone, Scotland, *J. Struct. Geol.*, *22*, 543–560.

Tenthorey, E., S. F. Cox, and H. F. Todd (2003), Evolution of strength recovery and permeability during fluid-rock reaction in experimental fault zones, *Earth Planet. Sci. Lett.*, *206*(1–2), 161–172.

Tenthorey, E., and S. F. Cox (2006), Cohesive strengthening of fault zones during the interseismic period: An experimental study, *J. Geophys. Res.*, *111*, B09202, doi:10.1029/2005JB004122.

Tullis, T. E., and J. D. Weeks (1987), Micromechanics of Frictional Resistance of Calcite, *Trans. AGU*, *65*, 405.

Tullis, T. E. (1988), Rock frictional constitutive behavior from laboratory experiments and its implications for an earthquake prediction field monitoring program, *Pure Appl. Geophys.*, *126*, 555–588.

van Noort, R., C. J. Spiers, and C. J. Peach (2006), Effects of orientation on the diffusive properties of fluid-filled grain boundaries during pressure solution, *Phys. Chem. Miner.*, *34*, 95–112, doi:10.1007/s00269-00006-00131-00269.

Weeks, J. D., and T. E. Tullis (1985), Frictional sliding of dolomite: A variation in constitutive behavior, *J. Geophys. Res.*, *90*, 7821–7826, doi:10.1029/JB090iB09p07821.

Yasuhara, H., C. Marone, and D. Elsworth (2005), Fault zone restrengthening and frictional healing: The role of pressure solution, *J. Geophys. Res.*, *110*, B06310, doi:10.1029/2004JB003327.

D. Elsworth, Department of Energy and Mineral Engineering, Pennsylvania State University, Hosier Bldg. 231, University Park, PA 16802, USA.

C. Marone, Department of Geosciences, Pennsylvania State University, Deike Bldg. 536, University Park, PA 16802, USA.

A. Niemeijer, Istituto Nazionale di Geofisica e Vulcanologia, Via di Vigna Murata 605, Rome 00143, Italy. (andre.niemeijer@ingv.it)